PAPER • OPEN ACCESS

Large-area zinc oxide nanorod arrays templated by nanoimprint lithography: control of morphologies and optical properties

To cite this article: Chen Zhang *et al* 2016 *Nanotechnology* **27** 485604

View the article online for updates and enhancements.

Related content

- The growth mechanism and optical properties of ultralong ZnO nanorod arrays with a highaspect ratio by a preheating hydrothermal method
  Jijun Qiu, Xiaomin Li, Weizhen He et al.

- Zinc oxide nanorod based photonic devices: recent progress in growth, light emitting diodesand lasers
  M Willander, O Nur, Q X Zhao et al.

- Position controlled and seed/catalyst free growth of ZnO nanorod arrays on reduced graphene oxide nanosheets
  Hui Yang, Jinliang Li, Lan Li et al.

Recent citations

- Magnetic and Photoluminescent Coupling in SrTi0.87Fe0.13O3/ZnO Vertical Nanocomposite Films
  Chen Zhang *et al*

Large-area zinc oxide nanorod arrays templated by nanoimprint lithography: control of morphologies and optical properties

Chen Zhang[1,2], Xiaohu Huang[3], Hongfei Liu[3], Soo Jin Chua[2,3] and Caroline A Ross[1]

[1] Department of Materials Science and Engineering, Massachusetts Institute of Technology, 77 Massachusetts Avenue, Cambridge, MA 02139, USA
[2] Singapore-MIT Alliance, National University of Singapore, 4 Engineering Drive 3, 117576 Singapore
[3] Institute of Materials Research and Engineering, 2 Fusionopolis Way, Innovis 138634, Singapore

E-mail: zhangch@mit.edu, elecsj@nus.edu.sg and caross@mit.edu

Abstract

Vertically aligned, highly ordered, large area arrays of nanostructures are important building blocks for multifunctional devices. Here, ZnO nanorod arrays are selectively synthesized on Si substrates by a solution method within patterns created by nanoimprint lithography. The growth modes of two dimensional nucleation-driven wedding cakes and screw dislocation-driven spirals are inferred to determine the top end morphologies of the nanorods. Sub-bandgap photoluminescence of the nanorods is greatly enhanced by the manipulation of the hydrogen donors via a post-growth thermal treatment. Lasing behavior is facilitated in the nanorods with faceted top ends formed from wedding cakes growth mode. This work demonstrates the control of morphologies of oxide nanostructures in a large scale and the optimization of the optical performance.

S Online supplementary data available from stacks.iop.org/NANO/27/485604/mmedia

(Some figures may appear in colour only in the online journal)

1. Introduction

One-dimensional zinc oxide (ZnO) nanostructures with precisely controlled position, morphology and physical properties are the key building blocks for novel photonic [1, 2], piezoelectric [3, 4], photovoltaic [5, 6], sensing [7] and data storage [8] devices. To fabricate ZnO nanorods, a common

approach is the vapour–liquid–solid (VLS) method [9], but this process requires additional assembly of metal catalyst particles to achieve precise registration of the nanorod growth sites. The use of a metal catalyst itself may also introduce contamination in the nanostructures and limit the choice of materials for device fabrication [10]. Alternatively, the catalyst-free and selective growth of ZnO nanorods using a lithographic process has been extensively demonstrated [11–15]. However, questions remain concerning the extent over which the morphology of nanorods can be controlled and the physical properties related to the specific morphology can in turn be tailored. Also, the capability to scale-up the

fabrication of highly ordered nanorod arrays has been limited due to the use of small-area lithographic techniques and the necessity for lattice-matched substrates. The control of the morphology and physical properties of large-scale templated nanorods on Si substrates and textured seed layers that contain defects such as dislocations and grain boundaries is still challenging but of high practical importance.

Although the chemistry of the solution growth of ZnO nanostructures has been well documented [16, 17], there is still a lack of fundamental understanding of their growth mechanism and morphology evolution. Recent progress on the growth of ZnO nanorod arrays has demonstrated the dependence of nanorod diameter on nanorod height [18] and subsequently the independent control of the nanorod length and diameter via rate-limiting regimes [19]. On the other hand, according to the Burton–Cabrera–Frank (BCF) theory [20], under low supersaturation, the crystals only grow when they contain screw dislocations. The spiral mounds formed from the screw dislocations exhibit conical shapes and ascending steps which converge on the spiral cores. Recently, screw-dislocation-driven spiral growth has been demonstrated in various systems including nanowires [21, 22], nanotubes [22] and nanoplates [23]. Simulations by Redinger *et al* predicted that 'wedding cakes', which often grow at low temperature and high supersaturation [24–26], are reminiscent of spirals despite a completely different growth mechanism [27]. Formation of both spiral and wedding cake mounds could be a general phenomenon in the growth of semiconductor nanostructures and it is important to experimentally determine which growth mode is indeed active. Moreover, solution-grown ZnO nanorods are known to suffer from poor functionality such as low near-band-edge (NBE) emission which prohibits practical applications in optoelectronic devices. A facile post-growth thermal treatment was demonstrated in this work to enhance the NBE emission through manipulation of hydrogen donors. Lasing behaviour was found to occur more easily in nanorods with smooth terraces that can be explained by the two-dimensional nucleation-driven wedding cake model.

2. Experimental method

2.1. Synthesis of textured ZnO seed layers

ZnO seed layers, ~70 nm in thickness, were grown on 2 inch Si wafers by pulsed laser deposition (PLD) and 4 inch Si wafers by radio-frequency (RF) magnetron sputtering. For PLD growth, the chamber was pumped down to a base pressure of 2×10^{-6} Torr before deposition. A KrF excimer laser at an operating wavelength of 248 nm was used as the ablating source. The pulses were repeated at a frequency of 10 Hz and the fluence was about 2.6 J cm^{-2}. An oxygen partial pressure of 5×10^{-3} Torr, substrate temperature of 600 °C, and target-to-substrate distance of 7 cm were maintained during the deposition. For RF sputtering growth, the chamber was pumped down to a base pressure of 4×10^{-7} Torr. Sputtering was performed at a constant power

of 60 W at working pressure of 5×10^{-3} Torr. The deposition temperature was set at 600 °C and the target-to-substrate distance was 10 cm.

### 2.2. Fabrication of nanoimprinted patterns

Wafer-scale resist patterns were created using step and flash nanoimprint lithography (S-FIL, Imprio 100). Ultraviolet (UV) curable monomer resist (Monomat) was dispensed on the selected area. A quartz template with nanopatterns was applied to the resist layer. The resist was attracted into the nanopatterns by capillary force and formed resist patterns after UV curing. By repeating the processes of dispensing, imprinting and exposure, patterns can be uniformly fabricated on 2 inch (PLD seed layer) and 4 inch (sputter seed layer) Si wafers. Large-area uniformity of the patterns was achieved by accurate levelling of the substrate and template. As surface roughness resulted in substantial deviation of the levelling along a large area, the textured-ZnO seedlayer coated on the Si wafers were also kept thin (<100 nm) to avoid large surface roughness. The residual resist layer was removed by reactive ion etching (RIE) in oxygen plasma (Oxford Plasma 80) to expose the seed layer underneath. After plasma etching for 20 s, the size of the resist holes increased laterally by ~30%.

2.3. Synthesis of ZnO nanorods

The patterned substrates were subsequently immersed in an aqueous solution at 90 °C in a water bath. The solution was prepared by dissolving 27 mM zinc acetate. The pH of the solution was adjusted to be approximately 10 by adding 0.15 M ammonia. The equilibrium concentration of the system is estimated to be 0.5 mM. For certain samples, 8 mM sodium citrate were added to impede to vertical growth of the nanorods. The growth time ranged from 10 min to 12 h. The fabrication process is schematically illustrated in figure S1 in the supplementary data. ZnO nanorods were also grown on GaN substrates as a comparison to investigate the growth mechanism. The single crystal GaN film was grown by metal–organic vapour phase epitaxy (MOCVD) on a sapphire substrate. The GaN film was *c*-axis orientated and the thickness was $2 \sim 3\ \mu$m. The dislocation density decreases as the thickness of GaN film increases. For the film thickness of $2 \sim 3\ \mu$m, the total dislocation density is $\sim 1 \times 10^9$ cm^{-2}.

2.4. Characterization of ZnO nanorods

Morphologies of the nanomaterials were characterized by atomic force microscopy (AFM, Multimode-Digital Instruments) and field-emission scanning electron microscopy (SEM, JEOL JSM6700F). The nanorod length was measured from the cross-section SEM images. The average length and standard deviation was obtained using ImageJ with the sample size of 10–12 nanorods. Structural characterization was carried out using a general area detector diffraction system (GADDS, Cu Kα, Bruker D8) and high resolution x-ray diffraction (XRD, Cu Kα, PANalytical X'Pert Pro). Microstructures and interfaces were studied using high resolution
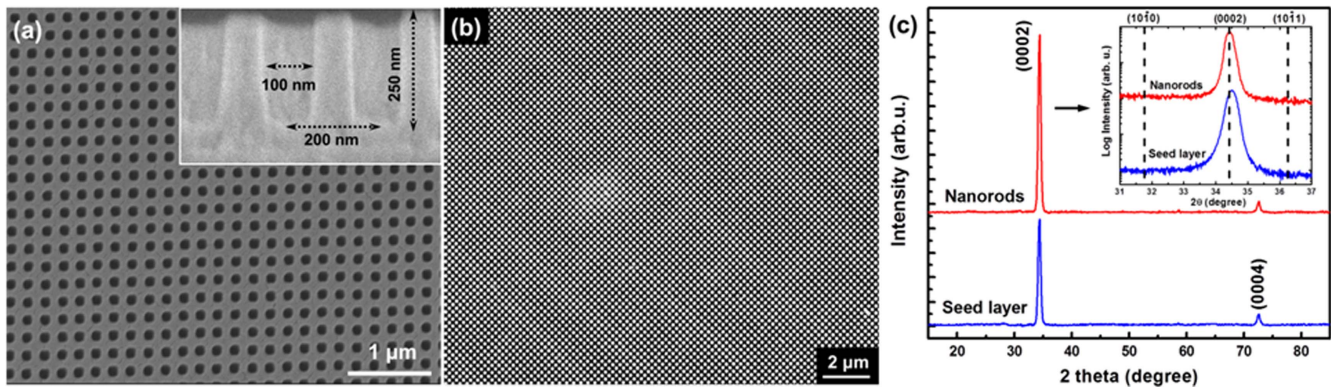
Figure 1. (a) SEM top view image of resist patterns formed on top of the seed layer with a cross-section view image in the inset. (b) SEM top view image of ZnO nanorod arrays over a large area. (c) XRD 2θ spectra of ZnO seed layer and nanorod arrays. The inset shows high resolution spectra near the ZnO (0002) diffraction peak. The dashed lines indicate the position of orientations for bulk ZnO (JCPDS No. 89-1397).

transmission electron microscopy (TEM, Philips CM300). The as-grown samples were annealed using a rapid thermal annealing system (RTA, ULVAC-RIKO MILA-3000). The annealing temperature was ramped at a rate of $35\,^{\circ}\mathrm{C\,s^{-1}}$, and then held constant for 30 min before being cooled down to room temperature at a rate of $60\,^{\circ}\mathrm{C\,min^{-1}}$. Optical properties of the samples were studied using micro-PL (Renishaw Ramanscope 2000) with a He-Cd laser ($\lambda = 325$ nm) as the excitation source. The optical pumping was performed at room temperature with samples excited by 35 fs pulses at 325 nm from an optical parametric amplifier (TOPAS-CTM). The pulses ($\sim 3\,\mu$J/pulse) were incident normally to the samples and focused onto a spot of $\sim 500\,\mu$m diameter. The luminescence was dispersed by a monochromator and detected with a CCD detector in a conventional back-scattering geometry.

3. Results and discussion

3.1. Morphology and structure of ZnO nanorods

The typical route to forming vertically aligned ZnO nanorod arrays on a lattice-mismatched Si substrate starts from the deposition of a textured ZnO seed layer by spin-coating and annealing of the precursors [28], but the degree of alignment of the resulting nanorods is limited. In order to obtain a perpendicular *c*-axis orientation of high uniformity, polycrystalline ZnO films (~ 70 nm thickness) were deposited on Si substrates by PLD and sputtering as seed layers. The RMS roughness for PLD and sputtered seed layers are 1.13 nm and 2.65 nm, and the grain sizes are 20.5 nm and 22.5 nm, respectively (see figure S2 in the online supplementary data). An array of cylindrical hole patterns were created on top of the seed layer by nanoimprint lithography, with diameter of 100 nm and aspect ratio of ~ 2.5:1, as shown in figure 1(a). After plasma etching, highly aligned ZnO nanorods were subsequently grown with large-area uniformity, as shown in figure 1(b). The orientations of the nanorods were controlled by the texture of the seed layer, as indicated by XRD θ–2θ spectra in figure 1(c). Both the seed layer and nanorods

showed a (0002) out-of-plane orientation. The ($10\bar{1}0$) and ($10\bar{1}1$) diffraction peaks which are commonly present in solution-grown ZnO nanorods are absent, suggesting the nanorods are highly aligned. The 2θ value of the (0002) diffraction peak for the seed layer was larger than that of the bulk ZnO and the nanorods. This is attributed to the seed layer being under in-plane tensile stress associated with island coalescence through a zipping process [29], in which the free surfaces of two islands merge to form a grain boundary through elastic distortion leading to strain energy.

The SEM top, cross-section and tilted views of the ZnO nanorods grown for 10 min are shown in figures 2(a)–(c), respectively. The surface topography of the nanorods is reminiscent of the grain structures of the seed layer and persists during growth. The top of the nanorods exhibit rounded shape. By adding sodium citrate surfactant into the solution, the vertical growth of the nanorods was effectively impeded. The possibility for the adatoms to incorporate near the grain boundaries of the textured polycrystalline seed layer increased and the coalescence of the grains is favoured. The morphology of the nanorods shows flat top ends and a single nanorod grows from each pattern hole without grains or branches visible, as depicted in figures 2(d)–(f). The drawbacks for adding surfactant include the limited length of the nanorods and increased defects. To study the morphologies of longer nanorods that exit the holes, ZnO nanorods were grown without surfactant for extended growth time. ZnO nanorods grown for 30 min on a PLD seed layer exhibit a branched structure but the top of the nanorods is faceted, as shown in figures 2(g)–(i). In contrast, ZnO nanorods grown on a sputtered seed layer for 30 min exhibit coalesced branches but rounded top ends without hexagonal facets, as shown in figures 2(j), (k). After 12 h growth, the nanorods fully coalesced into single faceted nanorods of $\sim 2\,\mu$m length, but the perpendicular alignment was degraded, as shown in figure 2(l).

The microstructure and interfaces are important in determining the properties of ZnO nanorods, but there is a lack detailed TEM assessment of the interfaces of ordered ZnO nanorod arrays on textured seed layers in previous
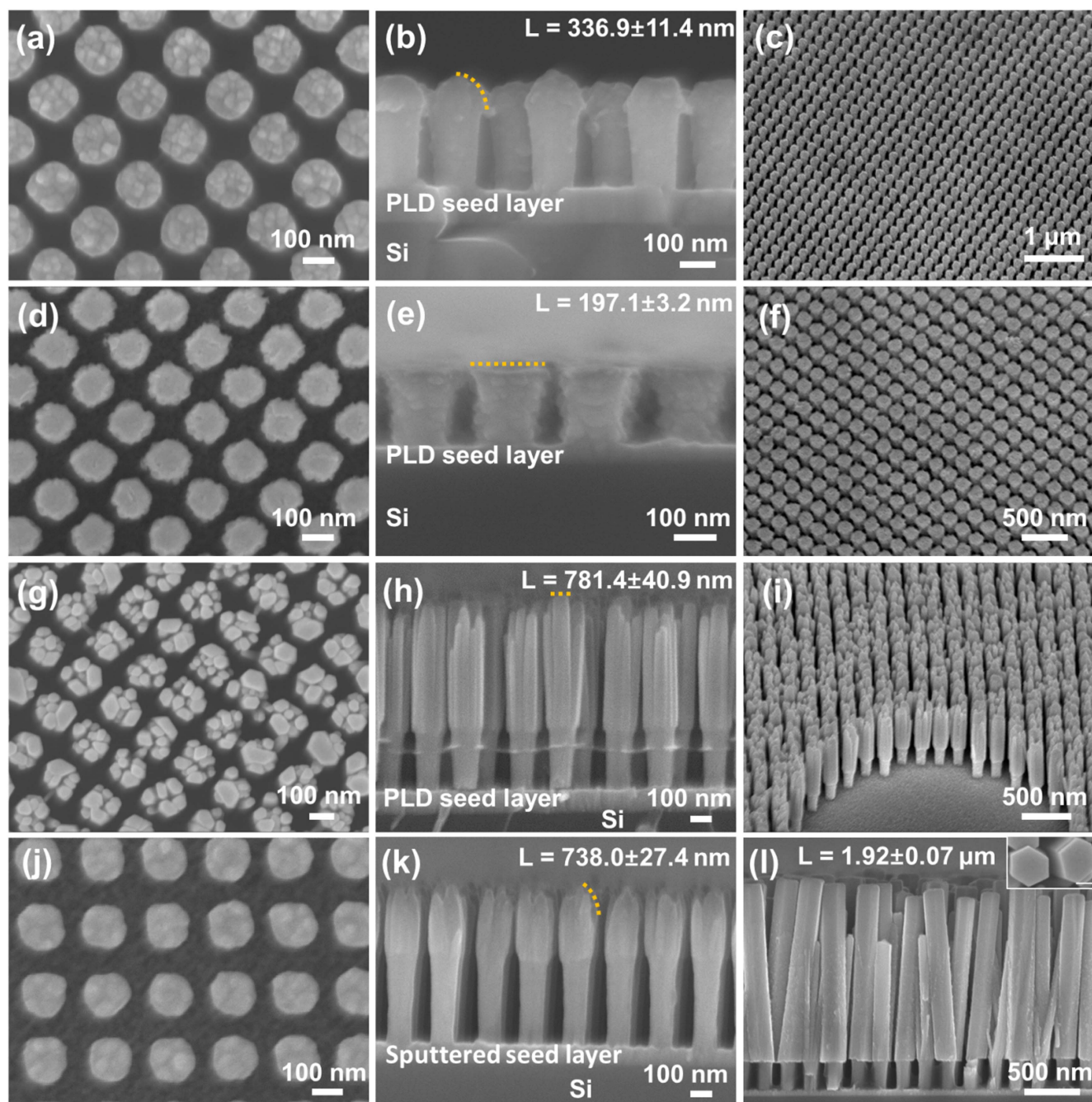
Figure 2. SEM (a) top, (b) cross-section and (c) tilted view of ZnO nanorods grown on PLD seed layer for 10 min. SEM (d) top, (e) cross-section and (f) tilted view of ZnO nanorods grown on PLD seed layer for 10 min with sodium citrate surfactant. SEM (g) top, (h) cross-section and (i) tilted view of ZnO nanorods grown on PLD seed layer for 30 min. SEM (j) top and (e) cross-section view of ZnO nanorods grown on sputtered seed layer for 30 min, (l) cross-section view of nanorods grown for 12 h. L indicates the length of the nanorods.

reports. A cross-section TEM image of a ZnO nanorod grown for 30 min on PLD seed layer is shown in figure 3(a). An amorphous SiO$_x$ layer of ~3 nm thickness existed between the Si substrate and the ZnO textured seed layer, as shown in figure 3(b). The interface between the nanorod and seed layer, as revealed in figure 3(c), was not clearly delineated, which indicates good epitaxy of the nanorod from the seed layer. The vertical edge of the rod surface illustrates effectiveness of the resist in controlling the sideways growth. Figure 3(d) shows fewer defects present at the upper region of a nanorod

compared to the interface region at the bottom of the rod. Selected area electron diffraction (SAED) patterns, as shown in figure 3(e), prove that the nanorods were ZnO single crystals with the wurtzite structure and *c*-axis orientation along their length.

3.2. Growth mechanism

We further focus on the nanorods grown for 30 min on PLD seed layer to study the mechanism that governs such morphologies. In a system at low temperature and high
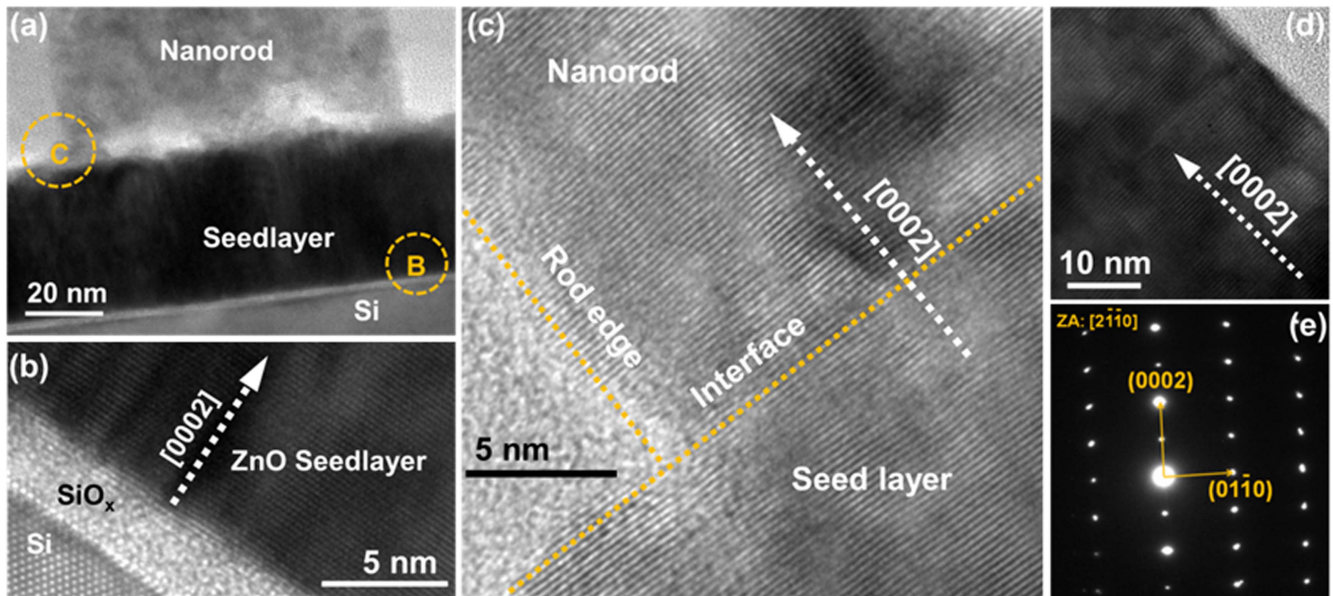
Figure 3. (a) TEM cross-section view image of a ZnO nanorod on a seed layer and on a Si substrate. (b) Interface of ZnO seed layer and Si substrate showing an intermediate amorphous SiO$_x$ layer. (c) HRTEM image of the nanorod-seed layer interface showing alignment of crystal orientations and a sharp rod edge. (d) HRTEM image of the nanorod showing the side wall and (e) SAED patterns.

growth rates, the diffusing adatoms can be reflected from descending step edges, preventing effective interlayer mass transport and leading to mound formation. This is understood by the presence of an additional energy barrier, known as the Ehrlich-Schwoebel barrier (ESB) [30, 31] at the step edges. When interlayer mass transport is suppressed by ESB, adatoms do not incorporate layer-by-layer but form wedding cake mounds by a two-dimensional (2D) nucleation process. According to classical thermodynamic theory, nucleation of the adatoms is thermally activated and a function of supersaturation. With the growth temperature kept constant at 90 °C, the driving force of nucleation is proportional to supersaturation, which is defined as:

$$\alpha_{SS} = \ln\left(\frac{c}{c_o}\right)$$

where c and c_o are the concentration and equilibrium concentration of the system, respectively [32]. As the supersaturation increases, the crystal growth is progressively dominated by dislocation growth, layer-by-layer growth and dendritic growth [33]. In ZnO solution growth on textured seed layers, mound formation is favoured due to the low growth temperature, presence of numerous nucleation sites and diffusion barriers, and high supersaturation.

Figure 4(a) shows a TEM image of ZnO nanorods scratched from the substrate and placed onto holey carbon grids. The magnified high resolution image of the top end of the nanorod showed structures consisting of descending steps with flat terraces which are characteristics of wedding cake mounds. In a separate experiment, ZnO nanorods were also grown on a GaN substrate as a comparison to further verify the growth mode. In figure 4(b), nanorods with flat terraces rather than spiral cores on the top facets were observed. The density of the nanorods was higher than the density of screw

and mixed type threading dislocations normally intersecting the GaN substrate surface, which are estimated to be ~3 screw dislocations per 10 μm^2 of surface [22]. Neither an axial dislocation propagating along the rod nor a spiral core at the top end was observed in HRTEM images. Figure 4(c) shows the SEM images of ZnO mounds formed on a textured ZnO seed layer without patterns. The magnified images indicate the coexistence of the wedding cake mounds (upper inset) and spirals (lower inset). Besides, after the top ends of nanorods growing above the top of the resist holes, the increasing of the overall diameter and tapering are observed in many nanorods, both of which are characteristic of a wedding cake growth mode. With this evidence, we suggest that both wedding cake mounds driven by 2D nucleation and spirals driven by screw dislocation may initiate the solution growth process of ZnO nanostructures, as schematically illustrated in figure 4(d). The adatom either diffuses on the terrace overcoming the diffusion barrier (E$_D$), or diffuses over the step edge with an extra energy of ESB (E$_{ES}$). Significant ESB suppresses interlayer mass transport and increases the density of adatoms on the top terrace. The nucleation rate is increased due to a higher probability of collisions between confined adatoms. Spirals are initiated at sites where screw dislocations intersect the substrate surface. The adatoms preferably incorporate at the jog formed by a screw dislocation to minimize the number of dangling bonds. The incorporation of an adatom creates a new jog leading to a self-perpetuating process. Figure 4(e) schematically illustrates the development of wedding cake-like ZnO nanorods from a nanoimprinted pattern. The grain boundaries from the polycrystalline seed layer act as a hard barrier which leads to a correspondence between the nanorod topography and the grain structures of the seed layer [34]. On the ascending steps at the side of the mounds, increasing coverage of the upper
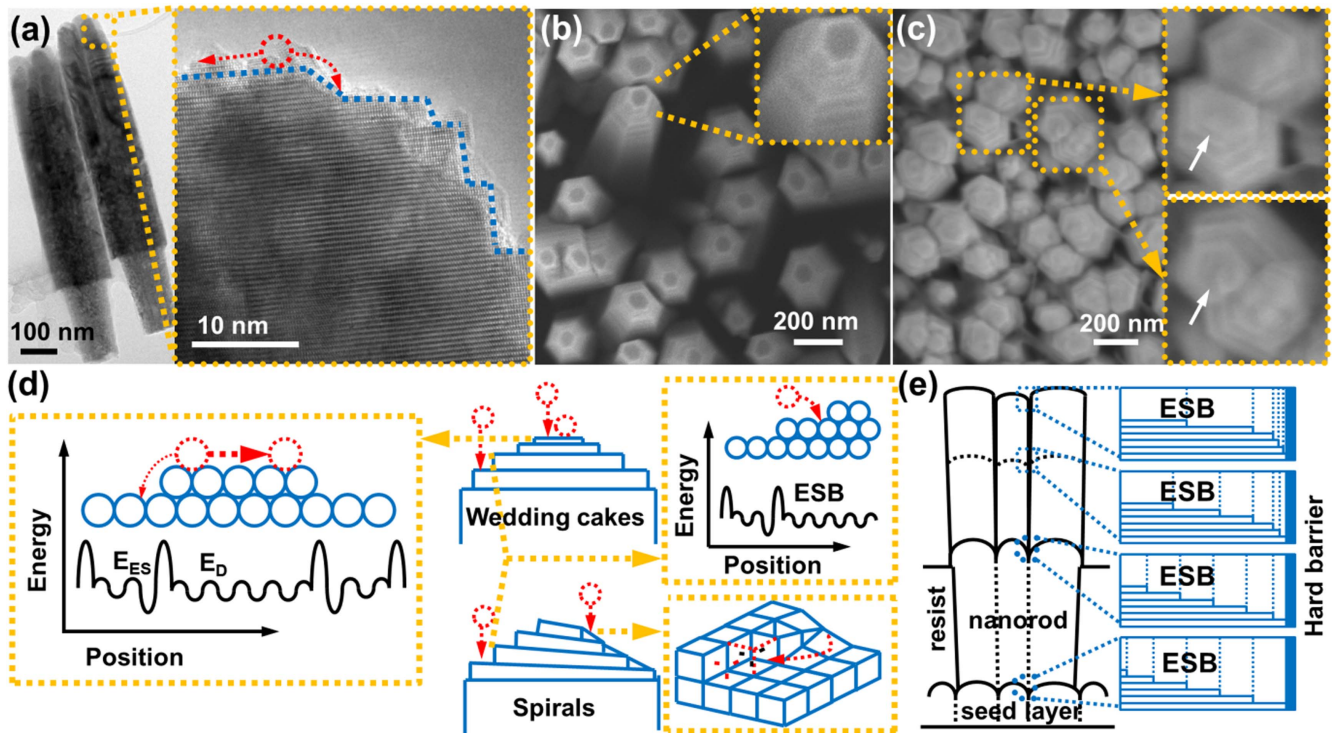
Figure 4. (a) TEM image of ZnO nanorods with magnified top region indicating the presence of steps and flat top terraces with a red circle denoting the adatom. (b) ZnO mounds formed on GaN substrate. (c) ZnO mounds formed on textured ZnO seed layer and Si substrate indicating the coexistence of wedding cake mounds and spirals. (d) Mechanism of mound formation for ZnO nanorod growth. (e) Evolution of surface morphologies and step coverage for patterned nanorod growth.
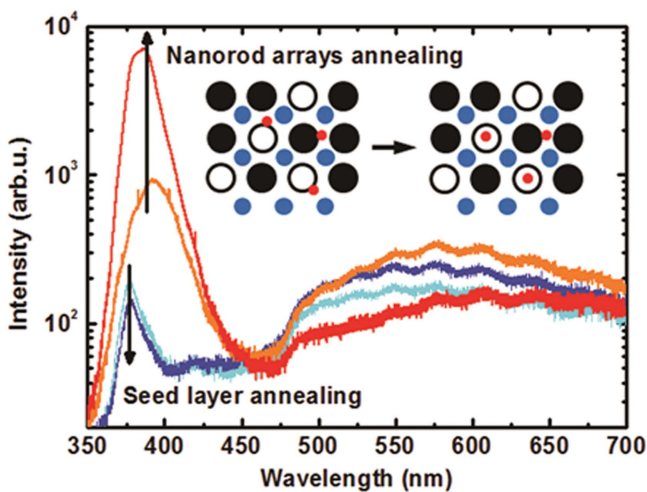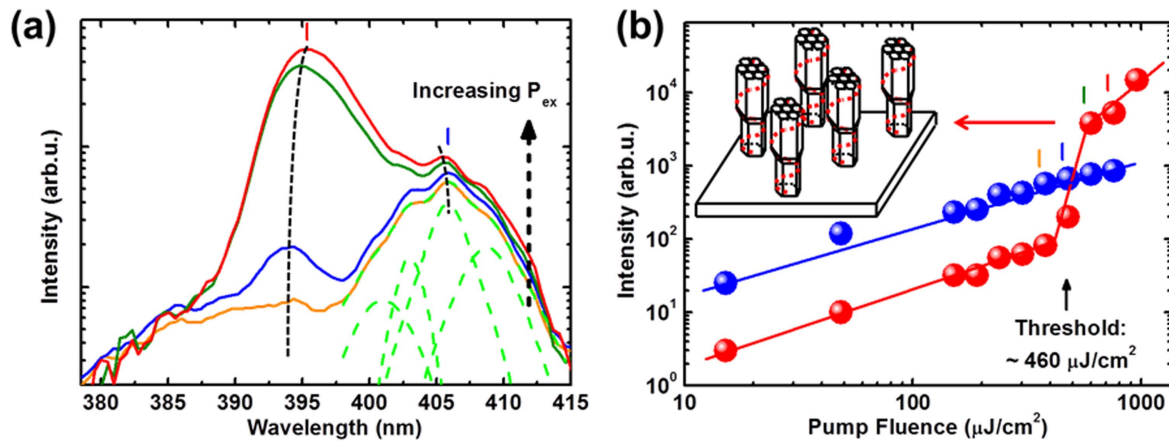

Figure 5. Room temperature PL spectra of as grown (orange) and annealed (red) ZnO nanorod arrays. PL spectra of as grown (cyan) and annealed (blue) plain ZnO seed layer obtained under the same conditions.

ledges reduces the step spacing near the edge of the mounds, resulting in a smaller chance for adatoms to arrive on the vicinal terraces and forming deep trenches [35, 36]. This is consistent with the observed branching effect of the nanorods even if the *c*-axis is perpendicular to the substrate surface.

3.3. Optical properties

The optical properties of the nanorods grown for 30 min on PLD seed layer with and without post-growth thermal treatment were studied. Figure 5 shows the room temperature PL spectra of as grown and annealed (425 °C, 10^{-4} Torr vacuum) samples of ZnO nanorod arrays. Suppression of deep level (DL) visible emission and pronounced enhancement of NBE UV emission were observed. The minimization of defect-related DL emission suggests improved crystallinity after annealing. The enhancement of NBE emission originates from the activation and dissociation of hydrogen donors induced by annealing in vacuum. The movement of the hydrogen donors is schematically illustrated in figure 5. A large amount of hydrogen interstitials existing in solution-grown ZnO nanorods moved into oxygen vacancy sites and contributed to excitonic recombination [37, 38], which was further identified by the I_4 peak from the low temperature PL spectra and Raman spectra (see figures S3, S4 in the supplementary data). In a separate measurement, the NBE emission intensity of the annealed nanorods is about two orders-of-magnitude larger than that of the bare seed layer, as shown in figure 5. The contribution of the seed layer to the optical properties of the nanorod arrays was therefore discounted.

The optical properties of the nanorod arrays can be tailored due to the different characteristic morphologies of the growth modes. As efficient guiding has been reported for ZnO nanostructures with diameters smaller than the wavelength of the guided light [39, 40]. ZnO nanorods grown on a PLD seed

Figure 6. (a) PL spectra of annealed ZnO nanorod arrays obtained under optical pumping at room temperature, with peaks at $\lambda = 394$ nm and $\lambda = 405.8$ nm corresponding to the lasing and LPB emissions respectively. (b) PL intensity of lasing (red) and lower polariton branch (blue) emissions versus pump fluence. The colours of the bars above each point correspond to the colours of the curves shown in (a). The inset schematically shows a possible way that the nanorod arrays act as coupled Fabry–Perot waveguide cavities.

layer showed smoother top facets (figures 2(h) and 4(a)) compared to the nanorods grown on a sputtered seed layer which exhibit rough nanorod/seedlayer interface and rounded top ends (figure S5 in online supplementary data). With smooth facets at the top and bottom acting as reflectors, each nanorod could behave as a Fabry–Perot-like waveguide cavity [41]. Also, for nanorods that mostly consist of wedding cake mounds with no screw dislocation at the centre along the longitudinal direction, there is less chance for non-radiative recombination to happen. Figure 6(a) shows the room temperature luminescence from the nanorod arrays grown for 30 min on a PLD seed layer excited with high power optical pulses. At low pump fluence (P_{ex}), a broad emission peak extended far below the bandgap of ZnO. It was resolved into four Lorentzian sub-peaks indicated by green dashed lines. As shown in figure 6(b), the intensity of the highest sub-peak at $\lambda \approx 405.8$ nm, increased linearly with P_{ex}. Originated from the lower polariton branch [40, 42], the strong light–matter coupling is not bleached at high P_{ex} probably due to smaller carrier density near the edge of the excitation spot [43]. As P_{ex} increased to a threshold value ($P_{ex} \approx 460 \, \mu J \, cm^{-2}$), additional sharp peaks at $\lambda \approx 394$ nm emerged and the intensity increased superlinearly with increasing P_{ex}. The output intensity tended towards a linear increase with excitation intensity for P_{ex} exceeding $\sim 600 \, \mu J \, cm^{-2}$. The intensity of the resulting peak was orders-of-magnitude higher than the spontaneous emission background and the dependence of output and excitation intensity exhibited a superlinear to a linear relationship, characteristics of stimulated emission. The linewidth was significantly larger than that of single nanorods, which is due to nanorod arrays forming multiple Fabry–Perot-like cavities. Superposition of peaks from cavities of slightly different length for the same longitudinal mode resulted in a spectrally broadened peak. The variation of the length is also illustrated by AFM section image in figure S6 in the online supplementary data. The mode spacing of the longitudinal Fabry–Perot waveguide is calculated by the

expression [44]:

$$\Delta\lambda = \frac{1}{L}\left[\frac{\lambda^2}{2}\left(n - \lambda\frac{dn}{d\lambda}\right)^{-1}\right]$$

where $L = 781.4$ nm is the mean cavity length, $n = 2.33$ is the refractive index at wavelength $\lambda = 394$ nm and $dn/d\lambda = -0.015 \, nm^{-1}$ is the chromatic dispersion. The mode spacing was calculated to be $\Delta\lambda \approx 12$ nm. In addition to the peak at $\lambda \approx 394$ nm, another waveguide mode should have been located at $\lambda \approx 382$ nm. The absence is due to the pronounced subwavelength guiding mediated mostly through exciton-photon coupling which results in very weak luminescence from the band edge and upper polariton branch [40]. Moreover, upon increasing P_{ex}, a blue-shift of the LPB emission is observed in figure 6(a), which is due to significant screening under higher excitation power. The red-shift of the lasing mode with increasing excitation power is attributed to band-gap renormalization and/or the increase of refractive index of ZnO caused by heat generated at higher excitation powers [39]. In contrast, no lasing behaviour was observed from nanorods grown on the sputtered seed layer which exhibit a rounded top surface. Our results suggest that nanorods ending with flat terraces developed from wedding cake growth mode facilitate efficient light guiding and lasing behaviour, which have important implications for nanolasers.

4. Conclusion

A method for creating large-scale and highly ordered ZnO nanorod arrays on Si substrate with controllable morphology and optical properties was demonstrated. The wedding cake mound formation was proposed in addition to the well-understood spiral growth to explain the observed features at the top of the ZnO nanorods. A better understanding of this mechanism can be generally useful for rational control of the morphologies and functionalities of nanomaterials. Strong NBE luminescence and lasing behavior observed from the

faceted ZnO nanorod arrays show promises of the nanorod arrays as miniaturized light emitters for optoelectronics, optogenetics and beyond.

References

[1] Huang X, Chen R, Zhang C, Chai J, Wang S, Chi D and Chua S J 2016 *Adv. Opt. Mater.* **4** 960
[2] Nguyen X S, Tay C B, Fitzgerald E A and Chua S J 2012 *Small* **8** 1204
[3] Wang Z L and Song J 2006 *Sci.* **312** 242
[4] Pradel K C, Wu W, Ding Y and Wang Z L 2014 *Nano Lett.* **14** 6897
[5] Jean J, Chang S, Brown P R, Cheng J J, Rekemeyer P H, Bawendi M G, Gradečak S and Bulović V 2013 *Adv. Mater.* **25** 2790
[6] Son D Y, Bae K H, Kim H S and Park N G 2015 *J. Phys. Chem.* C **119** 10321
[7] Huang H, Gong H, Chow C L, Guo J, White T J, Tse M S and Tan O K 2011 *Adv. Funct. Mater.* **21** 2680
[8] Song J, Zhang Y, Xu C, Wu W and Wang Z L 2011 *Nano Lett.* **11** 2829
[9] Yang P, Yan H, Mao S, Russo R, Johnson J, Saykally R, Morris N, Pham J, He R and Choi H J 2002 *Adv. Funct. Mater.* **12** 323
[10] Hemesath E R, Schreiber D K, Gulsoy E B, Kisielowski C F, Petford-Long A K, Voorhees P W and Lauhon L J 2012 *Nano Lett.* **12** 167
[11] Nicaise S M, Cheng J J, Kiani A, Gradečak S and Berggren K K 2015 *Nanotechnology* **26** 075303
[12] Byrne D, McGlynn E, Cullen J and Henry M O 2011 *Nanoscale* **3** 1675
[13] Richardson J J, Estrada D, DenBaars S P, Hawker C J and Campos L M 2011 *J. Mater. Chem.* **21** 14417
[14] Wei Y, Wu W, Guo R, Yuan D, Das S and Wang Z L 2010 *Nano Lett.* **10** 3414
[15] Hyoungwon P, Jae B K, Yeon Y K, Yeon C J and Heon L 2010 *Nanotechnology* **21** 355304
[16] Vayssieres L 2003 *Adv. Mater.* **15** 464
[17] Xu S and Wang Z L 2011 *Nano Res.* **4** 1013
[18] Lee J M, No Y S, Kim S, Park H G and Park W I 2015 *Nat. Commun.* **6** 6325
[19] Cheng J J, Nicaise S M, Berggren K K and Gradecak S 2015 *Nano Lett.* **16** 753
[20] Burton W K, Cabrera N and Frank F C 1951 *Phil. Trans. Roy. Soc. London* A **243** 299
[21] Bierman M J, Lau Y K, Kvit A V, Schmitt A L and Jin S 2008 *Sci.* **320** 1060
[22] Morin S A, Bierman M J, Tong J and Jin S 2010 *Sci.* **328** 476
[23] Morin S A, Forticaux A, Bierman M J and Jin S 2011 *Nano Lett.* **11** 4449
[24] Krug J, Politi P and Michely T 2000 *Phys. Rev.* B **61** 14037
[25] Krug J 1997 *J. Stat. Phys.* **87** 505
[26] Krug J 2002 *Physica* A **313** 47
[27] Redinger A, Ricken O, Kuhn P, Rätz A, Voigt A, Krug J and Michely T 2008 *Phys. Rev. Lett.* **100** 035506
[28] Greene L E, Law M, Tan D H, Montano M, Goldberger J, Somorjai G and Yang P 2005 *Nano Lett.* **5** 1231
[29] Floro J A, Hearne S J, Hunter J A, Kotula P, Chason E, Seel S C and Thompson C V 2001 *J. Appl. Phys.* **89** 4886
[30] Ehrlich G and Hudda F 1966 *J. Chem. Phys.* **44** 1039
[31] Schwoebel R L 1966 *J. Appl. Phys.* **37** 3682
[32] Ivan V 2003 *Crystal Growth for Beginners* (Singapore: World Scientific) (doi:10.1142/9789812796899)
[33] Jin S, Bierman M J and Morin S A 2010 *J. Phys. Chem. Lett.* **1** 1472
[34] Rost M J 2007 *Phys. Rev. Lett.* **99** 266101
[35] Elkinani I and Villain J 1993 *Solid State Commun.* **87** 105
[36] Pelliccione M, Karabacak T and Lu T M 2006 *Phys. Rev. Lett.* **96** 146105
[37] Huang X H, Tay C B, Zhan Z Y, Zhang C, Zheng L X, Venkatesan T and Chua S J 2011 *CrystEngComm* **13** 7032
[38] Huang X, Zhan Z, Pallathadka P K, Zhang C, Zheng L and Chua S J 2012 *CrystEngComm* **14** 5163
[39] Johnson J C, Yan H, Yang P and Saykally R J 2003 *J. Phys. Chem.* B **107** 8816
[40] Rühle S, Van Vugt L, Li H Y, Keizer N, Kuipers L and Vanmaekelbergh D 2008 *Nano Lett.* **8** 119
[41] Maslov A and Ning C 2003 *Appl. Phys. Lett.* **83** 1237
[42] Özgür U, Teke A, Liu C, Cho S J, Morkoç H and Everitt H O 2004 *Appl. Phys. Lett.* **84** 3223
[43] Guillet T, Brimont C, Valvin P, Gil B, Bretagnon T, Médard F, Mihailovic M, Zúñiga-Pérez J, Leroux M and Semond F 2011 *Appl. Phys. Lett.* **98** 211105
[44] Zimmler M A, Capasso F, Müller S and Ronning C 2010 *Semicond. Sci. Technol.* **25** 024001